Radiolabeled GPVI-Fc for PET Imaging of Multiple Extracellular Matrix Fibers: A New Look into Pulmonary Fibrosis Progression

Simon Isser[1], Andreas Maurer[1,2], Gerald Reischl[1,2], Martin Schaller[3], Irene Gonzalez-Menendez[2,4], Leticia Quintanilla-Martinez[2,4], Meinrad Gawaz[5], Bernd J. Pichler[1,2], and Nicolas Beziere[1,6]

[1]Werner Siemens Imaging Center, Department of Preclinical Imaging and Radiopharmacy, Eberhard Karls University of Tübingen, Tübingen, Germany; [2]Cluster of Excellence EXC 2180, "Image Guided and Functionally Instructed Tumor Therapies," Eberhard Karls University of Tübingen, Tübingen, Germany; [3]Department of Dermatology, University Medical Center, Eberhard Karls University of Tübingen, Tübingen, Germany; [4]Institute of Pathology and Neuropathology, Comprehensive Cancer Center, Eberhard Karls University of Tübingen, Tübingen, Germany; [5]Department of Cardiology and Angiology, University Hospital Tübingen, Eberhard Karls University of Tübingen, Tübingen, Germany; and [6]Cluster of Excellence EXC 2124, "Controlling Microbes to Fight Infections," Eberhard Karls University of Tübingen, Tübingen, Germany

Invariably fatal and with a particularly fast progression, pulmonary fibrosis (PF) is currently devoid of curative treatment options. Routine clinical diagnosis relies on breathing tests and visualizing the changes in lung structure by CT, but anatomic information is often not sufficient to identify early signs of progressive PF. For more efficient diagnosis, additional imaging techniques were investigated in combination with CT, such as ^{18}F-FDG PET, although with limited success because of lack of disease specificity. Therefore, novel molecular targets enabling specific diagnosis are investigated, in particular for molecular imaging techniques. **Methods:** In this study, we used a ^{64}Cu-radiolabeled platelet glycoprotein VI fusion protein (^{64}Cu-GPVI-Fc) targeting extracellular matrix (ECM) fibers as a PET tracer to observe longitudinal ECM remodeling in a bleomycin-induced PF mouse model. **Results:** ^{64}Cu-GPVI-Fc showed significant uptake in fibrotic lungs, matching histology results. Contrary to ^{18}F-FDG PET measurements, ^{64}Cu-GPVI-Fc uptake was linked entirely to the fibrotic activity of tissue and not was susceptible to inflammation. **Conclusion:** Our study highlights ^{64}Cu-GPVI-Fc as a specific tracer for ECM remodeling in PF, with clear therapy-monitoring and clinical translation potential.

Key Words: pulmonary fibrosis; PET; bleomycin

Pulmonary fibrosis (PF) is a fatal disease with a mean life expectancy of 3–5 y after diagnosis (1,2). It can originate from a myriad of factors such as age or exposure to chemicals and often rapidly progresses (3). Early identification of progressive forms of PF is crucial in populations presenting with interstitial lung diseases on CT. PF treatment outcome has been shown to significantly improve after an early treatment start (4), particularly since the only currently approved drugs against PF (pirfenidone and nintedanib) merely slow disease progression (5). Although PF is relatively easy to diagnose

clinically in its advanced stage despite unspecific symptoms due to the characteristic lung honeycombing visible on CT, early stages of progressive fibrosing interstitial lung disease remain difficult to identify (6). High-resolution CT can provide higher sensitivity and better recognition of abnormalities in potential PF patients than can regular CT, justifying its current central role in PF diagnosis (7,8), but early screening of interstitial lung disease populations cannot rely on high-resolution CT alone as it provides only a snapshot of anatomic structures. Accessing early biomarkers of the disease, ideally by imaging methods, might provide early screening of patients at risk of progressive fibrosing interstitial lung disease, as well as providing monitoring of disease progression and a novel way to assess treatment efficacy. ^{18}F-FDG PET imaging has shown moderate success in PF patients (9–11), as this radiotracer reflects only glucose uptake; cannot distinguish between inflammation, fibrosis, and malignant cell proliferation; and can thus provide misleading results.

In PF, tissue is remodeled through increased deposition of extracellular matrix (ECM) fibers such as collagen I–III, fibronectin, and fibrinogen, which mark disease onset and early progression. As such, these fibers represent ideal biomarkers for early PF diagnosis, and radiotracers targeting individual fibers such as collagen I have been developed and have shown promising results preclinically and clinically (12). However, no current radiotracers can provide an overall picture of ECM remodeling during progressive PF. Interestingly, with platelet glycoprotein VI (GPVI), nature provides a molecule able to target several ECM fibers, such as collagen I–III, fibronectin, and fibrinogen (13–15). GPVI is naturally expressed on the surface of platelets and megakaryocytes and plays a crucial role in their aggregation during wound repair due to its high affinity after dimerization for these ECM fibers (16,17). To capitalize on this high affinity, an IgG1 GPVI fusion protein (GPVI-Fc) mimicking highly affine GPVI dimers has been synthesized and initially investigated as an antithrombotic agent (18). Imaging using fluorescent GPVI-Fc and a ^{64}Cu-radiolabeled GPVI-Fc, ^{64}Cu-NOTA-GPVI-Fc (^{64}Cu-GPVI-Fc), showed the potential of this targeting vector in thrombosis imaging (19,20) as well as in several models presenting a fibrotic component such as rheumatoid arthritis and cutaneous delayed-type hypersensitivity reaction (21). Although some of these diseases are predominantly inflammatory, with fibrosis appearing at a later stage, tracer uptake might correlate with

changes in the ECM and be shown on in vivo imaging experiments and ex vivo histology.

In the current study, we investigated the potential of ^{64}Cu-GPVI-Fc for early detection of PF and monitoring of its progression in a bleomycin-induced PF mouse model. Our objective was to visualize and quantify progressive PF longitudinally, noninvasively, and with high disease specificity and to study the potential of the approach in comparison to ^{18}F-FDG PET imaging of PF.

MATERIALS AND METHODS

The full version of the Materials and Methods can be found in the supplemental materials (available at http://jnm.snmjournals.org). Figure 1 shows the study workflow.

Radiotracer Synthesis

^{18}F-FDG was produced using a TRACERlab MX module (GE Healthcare) with radiochemical purity of over 95%. ^{64}Cu-GPVI-Fc was produced as described previously with a radiochemical purity of over 95% (*21*). To perform isotype experiments, NOTA-GPVI-Fc was denatured according to the procedure developed by Akazawa-Ogawa et al. (*22*) by incubation for 30 min at 70°C and subsequently radiolabeled using the same procedure as with stock NOTA-GPVI-Fc with a radiochemical purity of over 70%. Denatured ^{64}Cu-GPVI-Fc is referred to here as radiolabeled isotype.

PF Model

Animal experiments were performed in accordance with the German Animal Protection Law protocols for animal use and care, approved by the Regierungspräsidium Tübingen (NTP-ID 00034862-5-7). In short, 1 mg of bleomycin per kilogram of body weight in 50 μL of saline was deposited intratracheally in 8-wk-old C57BL/6J female mice (50 μL of saline only in control animals) on day 0, following the procedure described by Walters and Kleeberger (*23*). For ethical reasons, animals losing more than 20% of their body weight or showing signs of significant suffering were euthanized and not included in the study. The group size for each experiment can be found in the supplemental materials.

PET and MRI

High-resolution PET scans were performed using Inveon small-animal PET scanners (Siemens Healthcare) with Inveon Acquisition Workplace software, version 2.1.272 (Siemens Medical Solutions). Tracers (1 per animal group) were injected in the tail vein (12 ± 1.2 MBq): ^{18}F-FDG was injected 5 s after the start of a 1-h dynamic scan followed by an 827-s transmission scan; ^{64}Cu-GPVI-Fc was imaged with a 10-min static scan at 3, 24, and 48 h after injection. Each PET scan was followed by MRI sequences for anatomic reference using a 7-T small-animal scanner (ClinScan; Bruker Biospin MRI GmbH) with Paravision software, version 6.0.1 (Bruker Corp.). PET images were coregistered with MR images using fiducial markers and analyzed with Inveon Research Workplace software (Siemens Healthcare) by drawing regions of interest on the MR images and applying them to the PET images for volumetric quantification of radiotracer accumulation in the entire lung for ^{64}Cu-radiotracer–injected animals and in the right lung lobes for ^{18}F-FDG–injected animals.

Biodistribution

The mice were killed using CO_2 and perfused with 20 mL of 4°C phosphate-buffered saline through the right ventricle. Organ samples were explanted for activity measurements ex vivo using a 2480 WIZARD^2 automatic γ-counter from PerkinElmer.

Histology

For hematoxylin and eosin and Masson trichrome staining, perfused lungs were fixated in formalin, embedded in paraffin, and cut into 5-μm-thick slices using a microtome (Leica). All samples were scanned with a Nanozoomer (Hamamatsu) and processed with CaseViewer (3DHISTECH). Photomicrographic images were acquired with an Axioskop 2 Plus microscope (Zeiss) equipped with a laser optic system (ProgRes C10 Plus camera; Jenoptik) and software. The final images were prepared with Adobe Photoshop CS6. Scoring of inflammation was based on hematoxylin- and eosin-stained sections as follows: 0 (no inflammation), 1 (mild inflammation), 2 (moderate inflammation), or 3 (prominent inflammation). Fibrosis was scored following the modified Ashcroft scale (*24*).

For fluorescence microscopy, frozen lung slices were labeled with antifibronectin, antifibrinogen, anticollagen I, anticollagen II, or anticollagen III primary antibodies. For secondary antibody, antirabbit Cy3 was used to visualize ECM fibers, and antihuman IgG-Cy5 was used to visualize NOTA-GPVI-Fc. Nuclei were stained using YO-PRO-1, and images were acquired using an LSM 800 system (Zeiss) with ZEN software (version 2.3, blue edition).

Data Evaluation and Statistics

Statistical analysis was performed using ordinary 1-way ANOVA (multiple-comparison test based on Dunnett correction) in GraphPad Prism, version 9.0.1. For comparison of lungs at different time points, groups were compared with the respective controls. For ex vivo biodistribution comparison of different organs, mixed-effects analysis was used, and groups were compared with the respective controls. For comparison between uptake of ^{64}Cu-GPVI-Fc and the radiolabeled isotype control, the unpaired *t* test was used. For histologic scoring evaluation, 2-way ANOVA was used. The results show each individual data point together with the mean of each group and its SD. γ-counter results from 1 mouse in the ^{18}F-FDG study were identified as an outlier by the Grubbs test, originating from a user error during ex vivo uptake measurement, and were removed from further statistical ex vivo evaluation.
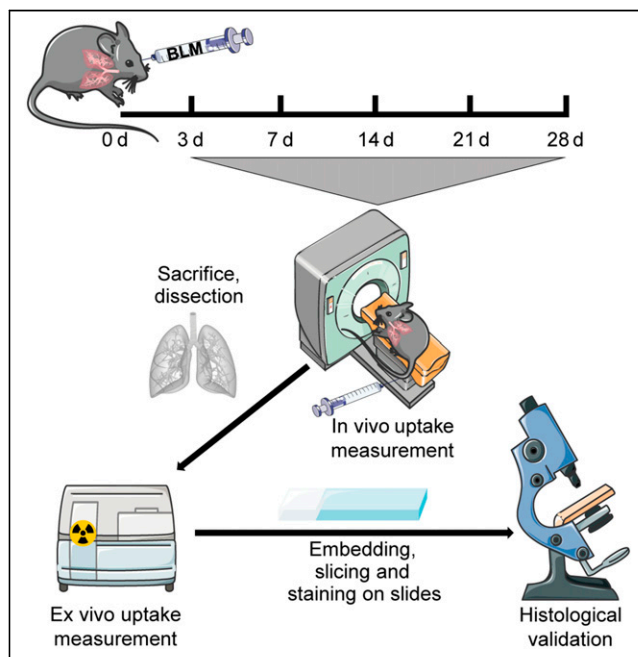
FIGURE 1. Experimental workflow for longitudinal PF imaging. Day 0: intratracheal deposition of bleomycin (BLM) or saline. Days 3, 7, 14, 21, and 28 after bleomycin deposition: PET and MRI scans after radiotracer injection. After in vivo imaging: euthanasia, biodistribution, microscopy imaging.
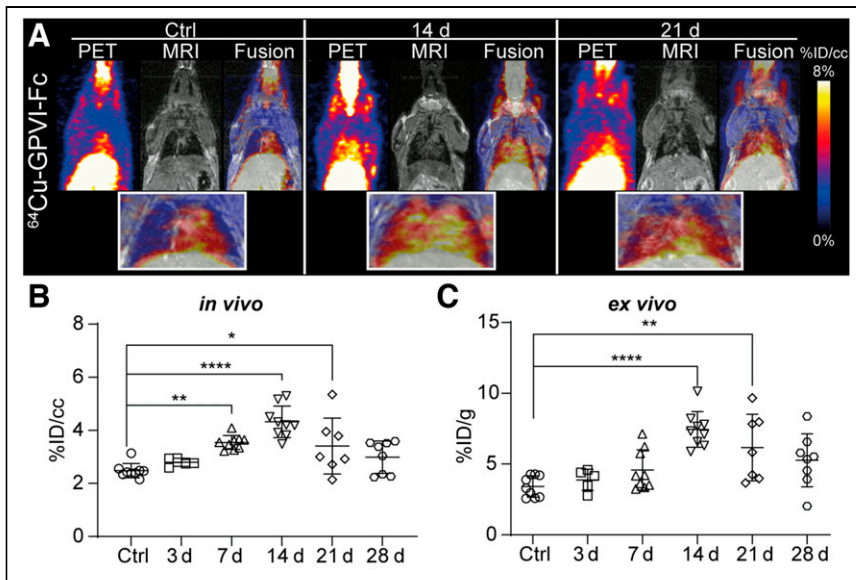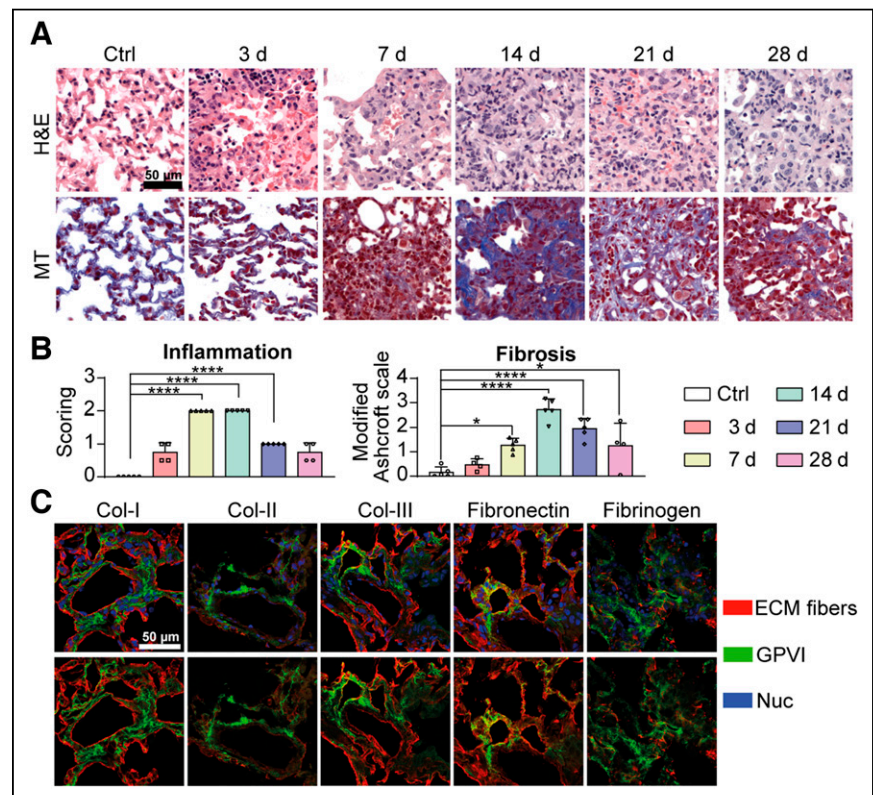
FIGURE 2. Representative images of ^{64}Cu-GPVI-Fc accumulation 48 h after radiotracer injection in animals that received intratracheal saline (control) or bleomycin 14 or 21 d after deposition. (A) Maximum-intensity-projection PET images fused with single-slice MR images ($n = 4$–9). (B) Corresponding quantification of in vivo tracer uptake in lungs. (C) Corresponding quantification of ex vivo tracer uptake in lungs. *$P \le 0.05$. **$P \le 0.01$. ****$P \le 0.0001$. Ctrl = control.

RESULTS

^{64}Cu-GPVI-Fc Imaging of PF Progression in Bleomycin Model

Imaging measurements were performed 3, 7, 14, 21, and 28 d after deposition of bleomycin (Fig. 1). ^{64}Cu-GPVI-Fc distribution was quantified during PF progression after MRI-guided organ segmentation to investigate ECM remodeling in bleomycin-exposed mice. Preliminary experiments performed 3, 24, and 48 h after injection of ^{64}Cu-GPVI-Fc indicated that the optimal uptake ratio in diseased animals could be attained 48 h after tracer injection (Supplemental Fig. 1). Pulmonary uptake of ^{64}Cu-GPVI-Fc 48 h after injection was visibly increased in vivo 7, 14, and 21 d after deposition compared with control (Fig. 2A). Quantification of in vivo measurements (Fig. 2B) showed no significant difference in radiotracer accumulation 3 d after deposition from that in control. Afterward, lung uptake was significantly higher than in control from 7 d after deposition, peaking at 14 d with a contrast ratio of 1.74, till 21 d after deposition (3.54 ± 0.26 percentage injected dose [%ID]/cm^3, 4.32 ± 0.60 %ID/cm^3, and 3.41 ± 1.06 %ID/cm^3, respectively). At 28 d after deposition, no significantly increased uptake compared with control was observed. Ex vivo measurement of ^{64}Cu-GPVI-Fc accumulation in the lungs confirmed a significantly higher uptake 14 and 21 d after

deposition than in control (7.44 ± 1.26 %ID/g, 6.17 ± 2.35 %ID/g, and 3.41 ± 0.75 %ID/g; $P \le 0.0001$ and $P \le 0.01$, respectively) (Fig. 2C). Analysis of ex vivo tracer biodistribution showed limited changes in other organs (Supplemental Fig. 2), with only the blood pool signal being lower 28 d after deposition than in control (2.45 ± 0.59 %ID/g to 2.91 ± 0.41 %ID/g, $P \le 0.05$). Pathologic changes were clearly visible in hematoxylin and eosin and Masson trichrome histology sections (Fig. 3A). Mild and focal inflammatory infiltrates were seen on day 3 after deposition, followed by more intense inflammatory infiltrates and minimal fibrosis on day 7. Fibrosis peaked at 14 d after deposition, followed by a small reduction in fibrotic areas at 21 and 28 d (Supplemental Fig. 3). Scoring (Fig. 3B) highlighted a significant increase in inflammation on days 7 (2.00 ± 0) and 14 (2.00 ± 0) after deposition, followed by a decline on day 21 (1.00 ± 0). Days 3 and 28 after deposition did not display a significant increase in immune cell infiltration compared with control. Modified Ashcroft scoring

**FIGURE 3.** (A) Hematoxylin and eosin and Masson trichrome staining in control animals and animals on days 3, 7, 14, 21, and 28 after bleomycin deposition. (B) Histologic scoring of inflammation and modified Ashcroft score ($n = 4$–5) in mouse lungs compared with controls. (C) Fluorescence microscopy for colocalization of GPVI-Fc with extracellular matrix fibers of collagen I–III and with fibronectin and fibrinogen. Nuclei stain added for cell localization. *$P \le 0.05$. ****$P \le 0.0001$. Col = collagen; Ctrl = control; ECM = extracellular matrix; H&E = hematoxylin and eosin; MT = Masson trichrome; Nuc = nuclei.
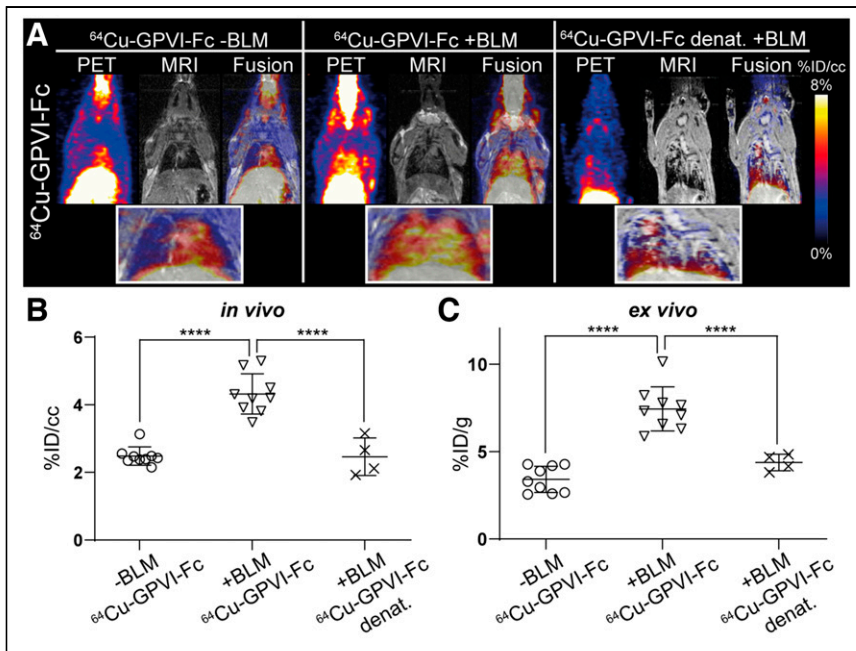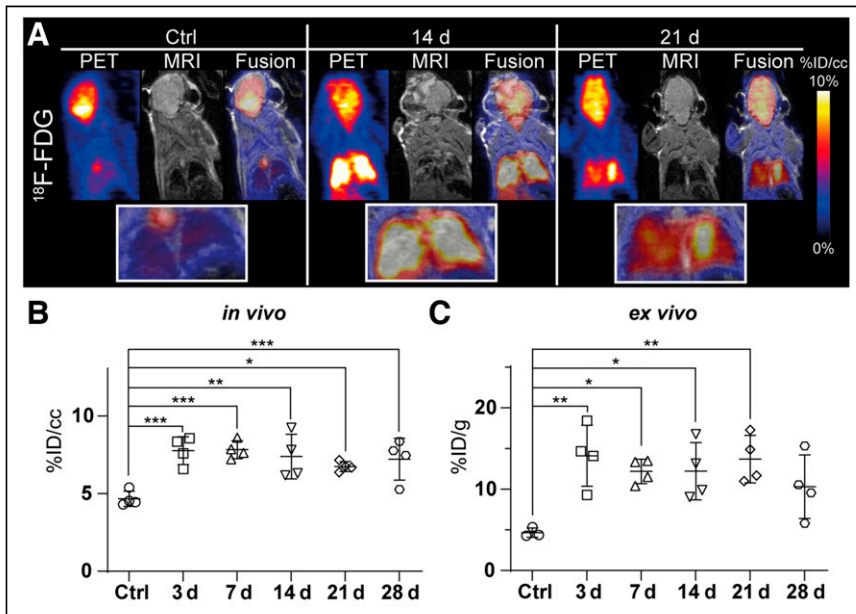
FIGURE 4. Uptake specificity of ^{64}Cu-GPVI-Fc. (A) Representative maximum-intensity-projection PET images fused with single-slice MR images 14 d after bleomycin deposition in control animals ($n = 9$), bleomycin-induced PF animals injected with ^{64}Cu-GPVI-Fc ($n = 9$), and bleomycin-induced PF animals injected with denatured ^{64}Cu-GPVI-Fc ($n = 4$). (B) Corresponding quantification of in vivo tracer uptake in lungs. (C) Corresponding quantification of ex vivo tracer uptake in lungs. ****$P \leq 0.0001$. -BLM = no bleomycin (control); +BLM = bleomycin-induced; denat. = denatured.

obtained from entire lung sections, comprising both healthy parenchyma and fibrotic areas, was higher than in control on day 7 after deposition (1.27 ± 0.28) but peaked on days 14 (2.72 ± 0.44) and 21

(1.96 ± 0.42). Day 28 after deposition presented a minor increase in fibrosis compared with control (1.29 ± 0.9). Fluorescence microscopy showed colocalization of GPVI-Fc and ECM fibers, such as collagen I–III, fibronectin, and fibrinogen, 14 d after deposition, with collagen III and fibronectin showing extensive colocalization (Fig. 3C).

Specificity of ^{64}Cu-GPVI-Fc for Fibrosis

To further investigate ^{64}Cu-GPVI-Fc specificity toward fibrosis in mouse lungs after bleomycin deposition, we performed binding experiments using a heat-denatured ^{64}Cu-radiolabeled GPVI-Fc (isotype). Decreased uptake of the isotype was visible 14 d after deposition compared with intact ^{64}Cu-GPVI-Fc (Fig. 4A) 48 h after tracer injection (2.46 ± 0.56 %ID/cm^3 to 4.32 ± 0.60 %ID/cm^3, $P < 0.0001$) (Fig. 4B), confirmed by ex vivo measurement (4.37 ± 0.48 %ID/g and 7.44 ± 1.26 %ID/g, $P \leq 0.0001$) (Fig. 4C). The radiolabeled isotype showed accumulation in diseased animals close to the accumulation of ^{64}Cu-GPVI-Fc in control animals. Ex vivo biodistribution (Supplemental Fig. 4) showed a significantly decreased uptake in all measured organs compared with intact ^{64}Cu-GPVI-Fc, except in the spleen, with a significantly increased uptake of the radiolabeled isotype compared with intact ^{64}Cu-GPVI-Fc (16.55 ± 3.93 %ID/g and 9.02 ± 2.43 %ID/g, $P \leq 0.05$).

^{18}F-FDG Imaging of PF in Bleomycin-Inoculated Mice

To visualize glucose metabolism during progression of PF, we used ^{18}F-FDG PET in a distinct set of animals as it is considered the reference radiotracer even in PF imaging research (Fig. 5A) (25). Quantification of radiotracer accumulation in vivo (Fig. 5B) showed a significantly increased uptake at all time points, remaining stable throughout the course of the experiment (4.70 ± 0.56 %ID/cm^3 in control and 7.77 ± 0.92 %ID/cm^3 on day 3, 7.82 ± 1.14 %ID/cm^3 on day 7, 7.39 ± 1.45 %ID/cm^3 on day 14, 6.74 ± 0.41 %ID/cm^3 on day 21, and 7.21 ± 1.46 %ID/cm^3 on day 28, with $P \leq 0.001$, $P \leq 0.001$, $P \leq 0.01$, $P \leq 0.05$, and $P \leq 0.01$, respectively). This behavior was also seen ex vivo (Fig. 5C) on days 3, 7, 14, and 21 after deposition (4.65 ± 0.58 %ID/g in control and 14.10 ± 3.74 %ID/g, 12.17 ± 1.49 %ID/g, 12.20 ± 3.52 %ID/g, and 13.70 ± 2.92 %ID/g, with $P \leq 0.01$, $P \leq 0.05$, $P \leq 0.05$, and $P \leq 0.01$) but not day 28 (10.30 ± 3.91 %ID/g). A complete biodistribution analysis, however, showed no difference in uptake in other organs

FIGURE 5. ^{18}F-FDG PET imaging of mice with bleomycin-induced PF. (A) Representative single-slice PET images fused with single-slice MR images 14 and 21 d after bleomycin deposition and in control animals ($n = 4$–5). (B) Mean in vivo tracer uptake in the right lung lobe. (C) Ex vivo tracer uptake in same lobe. *$P \leq 0.05$. **$P \leq 0.01$. ***$P \leq 0.001$.

(Supplemental Fig. 5). Blood glucose levels had no influence on ^{18}F-FDG uptake in this experiment (Supplemental Table 1).

DISCUSSION

In this study, we used PET imaging of the ECM fibers targeting radiotracer ^{64}Cu-GPVI-Fc to monitor fibrosis progression in a bleomycin murine model of PF, and we investigated its potential for early and specific diagnosis of the disease. We showed that the significantly increased pulmonary uptake of ^{64}Cu-GPVI-Fc found at 14 and 21 d after deposition aligned with both ex vivo biodistribution analysis and histologic validation, with Ashcroft scoring highlighting acute fibrosis during the second and third weeks of disease progression. These findings are in line with the reported PF progression in this model, with a second- and third-week peak fibrotic activity (23,26,27). Seven days after deposition, however, a small increase in ^{64}Cu-GPVI-Fc accumulation could be seen in vivo but not confirmed ex vivo. To dismiss the possibility of inflammation-driven ^{64}Cu-GPVI-Fc accumulation in bleomycin-deposited animals, as the bleomycin model shows early inflammation during the first 2 wk in contrast to the human presentation of the disease (23,26,27), we performed radiolabeled isotype experiments using heat-denatured GPVI-Fc. No specific lung accumulation of the isotype radiotracer could be seen in vivo 14 d after deposition, a time point presenting both fibrosis and inflammation. Although a signal coming from the heart could be seen in control and diseased animals using ^{64}Cu-GPVI-Fc, the isotype showed a reduction in heart signal, likely because of the overall reduced circulation time of the radiotracer due to denaturation of the Fc fragment of the protein. In addition, fluorescence microscopy highlighted colocalization of NOTA-GPVI-Fc with different ECM fibers, such as collagen I–III, fibronectin, and fibrinogen. Interestingly, radiotracer accumulation was reduced 28 d after deposition, as was Masson trichrome staining. This corresponds to the so-called resolution phase of the disease, characteristic of the bleomycin animal model (28). Taken together, these findings underline the specific binding potential of the tracer during progressive fibrosis and its accuracy to detect early PF progression in vivo.

As a reference point, ^{18}F-FDG experiments were performed in vivo following the same experimental plan. The increase in ^{18}F-FDG PET uptake at all time points after deposition, covering inflammatory and fibrotic stages in the mouse model, highlights the poor specificity of ^{18}F-FDG for PF, as ^{18}F-FDG merely reports glucose uptake regardless of its origin, including the inflammatory phase present during the first week of the bleomycin murine model. This finding showcases the potential of ^{64}Cu-GPVI-Fc for early and specific detection of progressive fibrosis. Achieving a good correlation between ^{18}F-FDG PET imaging and a positive PF diagnosis requires complex, expensive, and time-consuming measurements—impractical in clinical routine (10)—which might be avoided by the use of a specific radiotracer. Furthermore, changes in ^{18}F-FDG uptake were not detectable in a clinical study 3 mo after pirfenidone treatment (29), significantly limiting the use of ^{18}F-FDG in the clinic for early PF diagnosis and therapy monitoring and underlining the need for specific noninvasive detection of progressive PF.

Different tracers targeting ECM changes have been reported (30). In particular, collagen I–targeting PET showed a behavior similar to that of ^{64}Cu-GPVI-Fc, with similar results over time in vivo in mice (12). In addition, this collagen I tracer was used in rats (31), with results comparable to ours albeit with a shifted timeline

likely due to the difference in model species. ^{68}Ga-pentixafor, targeting CXCR4, a protein upregulated in cancer as well as during progressive PF, has shown promising results in clinical trials, including a correlation between evolution of uptake and pirfenidone treatment outcome (32). Significant work on the fibroblast activation protein highlighted its involvement in the progression of PF and initiated the use of fibroblast activation protein–targeted radiotracers for PF imaging (33), which are also leading to promising results in the clinic (34). In contrast, ^{64}Cu-GPVI-Fc targets multiple collagen subtypes (I, II, and III) as well as fibronectin and fibrinogen (13–15), which are found in lung fibrotic regions with high amounts of myofibroblasts and are known to synergize to drive ECM remodeling (35). Thus, ^{64}Cu-GPVI-Fc may provide an alternative, more complete view of disease progression, possibly allowing for earlier detection of progressive forms of PF.

CONCLUSION

Here, we showed that ^{64}Cu-GPVI-Fc displays specific uptake during the progressive stage of PF in the bleomycin mouse model but not during the initial inflammatory phase specific to the bleomycin model. This specific uptake was confirmed ex vivo and provides a new approach by targeting multiple ECM components, giving access to a broad picture of PF progression. Therefore, ^{64}Cu-GPVI-Fc represents a new tool to image PF progression in vivo, with high clinical translation potential, able to distinguish between progressive fibrosis and inflammation effectively.

DISCLOSURE

ACKNOWLEDGMENTS

KEY POINTS

QUESTION: Can ECM disruption be applied as an early marker to depict progressive PF in a preclinical mouse model using ^{64}Cu-GPVI-Fc PET imaging?

PERTINENT FINDINGS: A preclinical bleomycin-induced PF mouse model was studied longitudinally using PET imaging of ^{64}Cu-GPVI-Fc. The radiotracer showed high specificity toward the fibrotic phase of the disease model in vivo, as shown by histology and fluorescence microscopy ex vivo.

IMPLICATIONS FOR PATIENT CARE: ^{64}Cu-GPVI-Fc PET imaging might help in early stratification of patients showing interstitial lung disease on classic high-resolution CT and in identifying early signs of progressive fibrosis without an invasive biopsy, therefore leading to an earlier treatment start.

REFERENCES

1. King TE, Pardo A, Selman M. Idiopathic pulmonary fibrosis. *Lancet.* 2011;378: 1949–1961.

2. Chen X, Guo J, Yu D, Jie B, Zhou Y. Predictors of mortality in progressive fibrosing interstitial lung diseases. *Front Pharmacol.* 2021;12:754851.

3. Raghu G. Idiopathic pulmonary fibrosis: lessons from clinical trials over the past 25 years. *Eur Respir J.* 2017;50:1701209.

4. Antoniou KM, Symvoulakis EK, Margaritopoulos GA, Lionis C, Wells AU. Early diagnosis of IPF: time for a primary-care case-finding initiative? *Lancet Respir Med.* 2014;2:e1.

5. Finnerty JP, Ponnuswamy A, Dutta P, Abdelaziz A, Kamil H. Efficacy of antifibrotic drugs, nintedanib and pirfenidone, in treatment of progressive pulmonary fibrosis in both idiopathic pulmonary fibrosis (IPF) and non-IPF: a systematic review and meta-analysis. *BMC Pulm Med.* 2021;21:411.

6. Cottin V, Hirani NA, Hotchkin DL, et al. Presentation, diagnosis and clinical course of the spectrum of progressive-fibrosing interstitial lung diseases. *Eur Respir Rev.* 2018;27:180076.

7. Walsh SLF, Devaraj A, Enghelmayer JI, et al. Role of imaging in progressive-fibrosing interstitial lung diseases. *Eur Respir Rev.* 2018;27:180073.

8. Abu Qubo A, Capaccione KM, Bernstein EJ, Padilla M, Salvatore M. The role of radiology in progressive fibrosing interstitial lung disease. *Front Med (Lausanne).* 2022;8:679051.

9. Castiaux A, Van Simaeys G, Goldman S, Bondue B. Assessment of ^{18}F-FDG uptake in idiopathic pulmonary fibrosis: influence of lung density changes. *Eur J Hybrid Imaging.* 2018;2:27.

10. Fraioli F, Lyasheva M, Porter JC, et al. Synergistic application of pulmonary ^{18}F-FDG PET/HRCT and computer-based CT analysis with conventional severity measures to refine current risk stratification in idiopathic pulmonary fibrosis (IPF). *Eur J Nucl Med Mol Imaging.* 2019;46:2023–2031.

11. Ko UW, Yoon H-y, Lee SH, et al. The value of ^{18}F-FDG PET/CT in evaluating disease severity in idiopathic pulmonary fibrosis [abstract]. *Eur Respir J.* 2017; 50(suppl 61):PA850.

12. Désogère P, Tapias LF, Hariri LP, et al. Type I collagen–targeted PET probe for pulmonary fibrosis detection and staging in preclinical models. *Sci Transl Med.* 2017;9:eaaf4696.

13. Moroi M, Jung SM. Platelet glycoprotein VI: its structure and function. *Thromb Res.* 2004;114:221–233.

14. Induruwa I, Moroi M, Bonna A, et al. Platelet collagen receptor glycoprotein VI-dimer recognizes fibrinogen and fibrin through their D-domains, contributing to platelet adhesion and activation during thrombus formation. *J Thromb Haemost.* 2018;16:389–404.

15. Mangin PH, Onselaer MB, Receveur N, et al. Immobilized fibrinogen activates human platelets through glycoprotein VI. *Haematologica.* 2018;103:898–907.

16. Chen H, Locke D, Liu Y, Liu C, Kahn ML. The platelet receptor GPVI mediates both adhesion and signaling responses to collagen in a receptor density-dependent fashion. *J Biol Chem.* 2002;277:3011–3019.

17. Jung SM, Moroi M. Platelet glycoprotein VI. *Adv Exp Med Biol.* 2008;640:53–63.

18. Ungerer M, Rosport K, Bultmann A, et al. Novel antiplatelet drug Revacept (dimeric glycoprotein VI-Fc) specifically and efficiently inhibited collagen-induced platelet aggregation without affecting general hemostasis in humans. *Circulation.* 2011;123:1891–1899.

19. Bigalke B, Lindemann S, Schonberger T, et al. Ex vivo imaging of injured arteries in rabbits using fluorescence-labelled glycoprotein VI-Fc. *Platelets.* 2012;23:1–6.

20. Bigalke B, Phinikaridou A, Andia ME, et al. Positron emission tomography/computed tomographic and magnetic resonance imaging in a murine model of progressive atherosclerosis using ^{64}Cu-labeled glycoprotein VI-Fc. *Circ Cardiovasc Imaging.* 2013;6:957–964.

21. Beziere N, Fuchs K, Maurer A, et al. Imaging fibrosis in inflammatory diseases: targeting the exposed extracellular matrix. *Theranostics.* 2019;9:2868–2881.

22. Akazawa-Ogawa Y, Nagai H, Hagihara Y. Heat denaturation of the antibody, a multi-domain protein. *Biophys Rev.* 2018;10:255–258.

23. Walters DM, Kleeberger SR. Mouse models of bleomycin-induced pulmonary fibrosis. *Curr Protoc Pharmacol.* 2008:46.

24. Hubner RH, Gitter W, El Mokhtari NE, et al. Standardized quantification of pulmonary fibrosis in histological samples. *Biotechniques.* 2008;44:507–511, 514–507.

25. Mahmutovic Persson I, von Wachenfeldt K, Waterton JC, Olsson LE; on behalf of the Tristan Consortium. Imaging biomarkers in animal models of drug-induced lung injury: a systematic review. *J Clin Med.* 2020;10:107.

26. Mouratis MA, Aidinis V. Modeling pulmonary fibrosis with bleomycin. *Curr Opin Pulm Med.* 2011;17:355–361.

27. Moore BB, Hogaboam CM. Murine models of pulmonary fibrosis. *Am J Physiol Lung Cell Mol Physiol.* 2008;294:L152–L160.

28. Tashiro J, Rubio GA, Limper AH, et al. Exploring animal models that resemble idiopathic pulmonary fibrosis. *Front Med (Lausanne).* 2017;4:118.

29. Bondue B, Castiaux A, Van Simaeys G, et al. Absence of early metabolic response assessed by ^{18}F-FDG PET/CT after initiation of antifibrotic drugs in IPF patients. *Respir Res.* 2019;20:10.

30. Désogère P, Montesi SB, Caravan PJCAEJ. Molecular probes for imaging fibrosis and fibrogenesis. *Chemistry.* 2019;25:1128–1141.

31. Mahmutovic Persson I, Fransén Pettersson N, Liu J, et al. Longitudinal imaging using PET/CT with collagen-I PET-tracer and MRI for assessment of fibrotic and inflammatory lesions in a rat lung injury model. *J Clin Med.* 2020;9:3706.

32. Derlin T, Jaeger B, Jonigk D, et al. Clinical molecular imaging of pulmonary CXCR4 expression to predict outcome of pirfenidone treatment in idiopathic pulmonary fibrosis. *Chest.* 2021;159:1094–1106.

33. Lindner T, Loktev A, Altmann A, et al. Development of quinoline-based theranostic ligands for the targeting of fibroblast activation protein. *J Nucl Med.* 2018;59: 1415–1422.

34. Röhrich M, Leitz D, Glatting FM, et al. Fibroblast activation protein–specific PET/CT imaging in fibrotic interstitial lung diseases and lung cancer: a translational exploratory study. *J Nucl Med.* 2022;63:127–133.

35. Herrera J, Henke CA, Bitterman PB. Extracellular matrix as a driver of progressive fibrosis. *J Clin Invest.* 2018;128:45–53.